Materials Science in Semiconductor Processing 219 (2027) 111332

Contents lists available at ScienceDirect

Materials Science in Semiconductor Processing

journal homepage: www.elsevier.com/locate/mssp

Unlocking the full potential of SSRM for GaAs: Nanoscale carrier profiling in nano-ridge laser diodes

L. Wouters [a,*], P. Lagrain [a], N. Peric [a], P.Y. Hsieh [a], P. Swekis [a], A.M.R. Sharma [a,b], Y. Mols [a], I. De Wolf [a,b], B. Kunert [a], T. Hantschel [a]

[a] Imec, Kapeldreef 75, 3001, Leuven, Belgium
[b] Dept. Materials Engineering, KU Leuven, 3001, Leuven, Belgium

ARTICLE INFO

Keywords:
SSRM
GaAs
Carrier profiling
Laser diode
Nano-ridge engineering
RTS SSRM

ABSTRACT

Owing to its direct bandgap and high electron mobility, gallium arsenide (GaAs) plays a key role in the development of high-performance electronic and optoelectronic devices. Accordingly, the accurate characterization of two-dimensional carrier distributions is essential to support their integration. Scanning spreading resistance microscopy (SSRM) is a well-established method for quantitative carrier profiling in silicon, while its application to III-V semiconductors is complicated by the non-ohmic nature of the tip-sample contact. Therefore, we present a systematic study of SSRM on GaAs, focusing on the optimization of both electrical (bias) and mechanical (force and repeated scanning) measurement conditions. Key performance metrics, including dynamic range, doping sensitivity, and repeatability, are evaluated to assess measurement reliability. Building on these insights, we demonstrate the applicability of SSRM to advanced nanoscale devices through a case study supporting the growth optimization of monolithically integrated GaAs nano-ridge laser diodes on silicon. The complex geometry and facet-dependent growth in these structures lead to non-trivial active dopant distributions, making them an ideal platform to highlight the capabilities of SSRM. Finally, we extend the use of SSRM to failure analysis by leveraging the reverse tip sample (RTS) methodology for site-specific electrical characterization of electrical stress-induced localized degradation defects in aged GaAs-on-Si laser diodes. In summary, this work establishes SSRM as a powerful technique for quantitative two-dimensional carrier profiling in both n- and p-type GaAs and demonstrates its value for the development, optimization, and failure analysis of advanced GaAs-based devices.

1. Introduction

Gallium arsenide (GaAs) is a prominent III–V semiconductor, valued for its direct bandgap of 1.42 eV in the technologically relevant near-infrared range, along with its high electron mobility, excellent thermal stability, and compatibility with bandgap engineering through III–V alloying [1]. These key properties have led to the development of a large variety of high-performance GaAs-based devices, such as laser diodes, photodetectors, heterojunction bipolar transistors, high-efficiency solar cells, and high-speed electronics [2–4]. Despite these advantages, as in all semiconductor devices, their performance critically relies on the precise control of carrier distribution at the nanoscale. While a wide range of characterization techniques for dopant profiling exist, high-resolution spatial mapping of carrier distributions in advanced semiconductor devices remains challenging [5].

For GaAs in particular, the capabilities and limitations of available dopant and carrier profiling techniques have been reviewed by Clarysse et al. [6]. For instance, dopant profiling in homogeneous GaAs layers with secondary ion mass spectrometry (SIMS) is mature and routinely applied [7,8]. Notably, the self-focusing SIMS concept coupled with Orbitrap mass spectrometry has recently extended SIMS analysis to nanometer-scale InGaAs/GaAs fin-array structures [9]. Despite this, SIMS remains fundamentally a depth-profiling technique and provides the total chemical dopant concentration, without direct information on the spatial distribution of electrically active carriers. Such information in III-V materials is commonly obtained through electrochemical capacitance-voltage (ECV) profiling, yet this technique shares the intrinsic limitation of one-dimensional profiling [10]. Atom probe tomography (APT) is a promising candidate for future 3D elemental mapping with near-atomic spatial resolution, but its application to GaAs

This article is part of a special issue entitled: GADEST 2026 published in Materials Science in Semiconductor Processing.

* Corresponding author.
E-mail address: lennaert.wouters@imec.be (L. Wouters).

https://doi.org/10.1016/j.mssp.2026.111332
Received 30 June 2026; Received in revised form 28 September 2026; Accepted 21 October 2026
Available online 4 November 2026
1369-8001/© 2026 The Authors. Published by Elsevier Ltd. This is an open access article under the CC BY-NC license (http://creativecommons.org/licenses/by-nc/4.0/).

and other III-V materials remains limited and is further constrained to the inherently small analysis volume of the needle-shaped specimen [11]. For two-dimensional mapping of electrically active carriers, one must currently rely on atomic force microscopy (AFM)-based methods such as scanning capacitance microscopy (SCM) and scanning spreading resistance microscopy (SSRM) [12]. Among these techniques, SSRM offers superior spatial resolution, high sensitivity over multiple decades, and a relatively straightforward calibration procedure, and will therefore be considered in greater detail below [13].

SSRM has become a well-established technique for both qualitative and quantitative electrical characterization of silicon (Si) structures and devices. It is primarily valued for its nanoscale spatial resolution, which arises from the formation of a metallic β-Sn phase within a nanometric volume beneath the tip, typically smaller than the tip radius itself. This phase transformation is induced by the GPa level contact pressures generated at the tip–sample interface during scanning and is responsible for the reduction in tip-sample contact resistance. As a result, the measured signal is dominated by the spreading resistance, which reflects the local resistivity and carrier concentration, thereby enabling quantitative carrier profiling in silicon-based materials [14]. For III-V materials, the β-Sn phase does not exist, and the tip-sample contact remains largely Schottky-like. Consequently, the measured resistance represents a convolution of spreading and contact resistances, complicating a direct correlation with the carrier concentration.

A detailed study of the current transport mechanisms between a diamond SSRM tip and doped GaAs and InP samples was reported by Lu et al. [15]. Under forward bias conditions, thermionic emission dominates, resulting in a strong positive correlation between SSRM current and carrier concentration for both n- and p-type GaAs, demonstrating the potential for quantitative carrier profiling. Under reverse bias and low doping conditions, however, generation-recombination currents dominate, causing a reversal of this correlation below 3×10^{17} cm^{-3} in p-type GaAs and an even more pronounced, bias-dependent inversion in n-type GaAs. In addition, other studies have reported repeatability issues, specifically for n-type GaAs [16]. Nevertheless, quantitative SSRM has been demonstrated, for instance through calibrated measurements of carrier profiles in thick p-type epilayers and n-type GaAs layers in heterojunction bipolar transistor (HBT) structures [6,17,18]. Overall, prior work indicates that quantitative SSRM analysis of GaAs is feasible but requires careful use of calibration standards and control of bias conditions, and has so far been mostly limited to one-dimensional profiling in laterally homogeneous structures.

In this work, we extend the current understanding of SSRM on GaAs by a systematic study of the optimal measurement conditions beyond the electrical tip-sample bias alone. In particular, we examine the influence of mechanical tip-sample interaction, including the applied force and the effects of repeated scanning, which are shown to be critical for reliable quantitative analysis. Furthermore, key performance metrics such as dynamic range, doping sensitivity, repeatability, and reproducibility are evaluated to assess the robustness of SSRM measurements on GaAs. Building on these insights, and in contrast to previous studies restricted to one-dimensional profiling, we demonstrate the applicability of SSRM for fully quantitative two-dimensional carrier mapping in complex nanoscale device architectures comprising both n- and p-type regions. This capability is illustrated through a case study in which SSRM has supported the development of monolithically integrated GaAs-based nano-ridge laser diodes on silicon, representing a promising step toward scalable integration of light sources for silicon photonics [19].

2. Samples & methods

We first introduce the GaAs calibration samples used to determine optimal measurement conditions and to define key performance metrics for SSRM on GaAs. We then present the GaAs nano-ridge laser diode structures and highlight the importance of two-dimensional carrier profiling by SSRM for their successful integration. Finally, the experimental details of the SSRM characterization, including sample preparation, are described.

2.1. GaAs calibration samples

The GaAs calibration samples are metal-organic vapor phase epitaxy (MOVPE)-grown multilayer stacks on semi-insulating GaAs substrates, comprised of layers covering a wide doping range, for both conductivity types. The n-type and p-type GaAs calibration samples are doped with silicon and zinc atoms, respectively. The individual layers have a thickness of approximately 1.5 μm and the electrically active carriers in each layer are determined by ECV profiling, yielding a staircase-shaped concentration profile, ranging from 2×10^{17} to 2×10^{20} cm^{-3} for p-type GaAs and 1×10^{17} to 8×10^{18} cm^{-3} for n-type GaAs. These calibration samples will be used as reference samples to investigate the SSRM behavior on GaAs and for resistance-to-carrier conversion in the GaAs nano-ridge device structures throughout this study. They will be referred to as Staircase P and Staircase N.

2.2. GaAs nano-ridge samples

The GaAs nano-ridge structures used in this work are deposited *via* MOVPE on pre-patterned 300 mm (001) Si substrates inside V-shaped Si {111} terminated oxide trenches using a nano-ridge engineering (NRE) approach. Selectively growing GaAs inside these narrow oxide trenches, enables defect reduction through aspect ratio trapping before continuing the deposition outside the trenches to increase the III-V nano-ridge volume [20]. In this approach, the lower part of the nano-ridge, confined within the trench, primarily serves to trap threading dislocations originating from the lattice mismatch between Si and GaAs while also preventing the formation of anti-phase boundaries [21]. As a result, significantly improved GaAs material quality is achieved in the upper part of the structure with increased nano-ridge dimension, where the active device region is formed as a vertically stacked p-i-n laser diode. Fig. 1a shows a schematic of the GaAs nano-ridge laser diode cross-section, accompanied by a high-resolution high-angle annular dark-field scanning transmission electron microcopy (HAADF-STEM) image in Fig. 1b.

The bulk nano-ridge region contains the active InGaAs multi-quantum-well (MQW) structure, embedded in an undoped GaAs layer, hereafter referred to as the intrinsic (i-GaAs) region. This heterostructure defines the gain medium of the laser, providing carrier confinement and enabling efficient radiative recombination. The outer InGaP surface passivation layer also enhances the carrier confinement and is intended to reduce surface recombination, thereby suppressing carrier losses at the nano-ridge surface. The n-type GaAs bottom region and p-type GaAs top region serve as electron and hole injection layers, respectively, with silicon and carbon used as the n- and p-type dopants. Higher doping reduces the contact resistance at both contacts, facilitating efficient carrier injection, but also introduces optical losses due to free-carrier absorption. In addition, the doping in these regions must be carefully engineered to shape the electric field distribution in the nano-ridge for efficient carrier transport toward the quantum wells. This explains the presence of a thicker p-GaAs layer transitioning to a thin p^+-GaAs contact layer. Tungsten contact plugs connect the top p-GaAs and bottom n-GaAs regions to separate copper contact lines (n-contact plug through the n^+-Si, not included in the schematic), allowing to electrically drive the p–i–n diode and enable carrier injection for laser operation.

The successful growth of a functional laser diode critically depends on both controlled nano-ridge geometry evolution out of the trench via NRE and on the controlled incorporation and activation of dopants within the evolving structure. Achieving such control is particularly challenging, as growth around three-dimensional structures leads to the formation of multiple crystallographic facets with different orientations

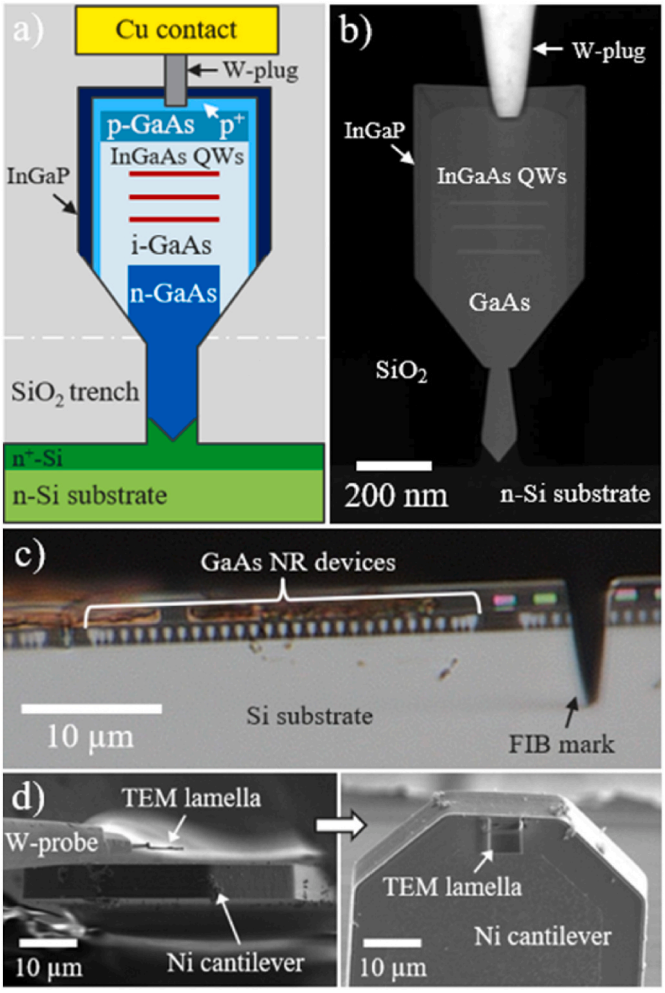


Fig. 1. a) Schematic cross-section of a GaAs nano-ridge laser device, highlighting the different layers; (b) HAADF-STEM image providing accurate feedback on the device geometry and clear material contrast; (c) Optical microscope image of the cleaved nano-ridge sample cross-section where SSRM measurements are performed; (d) TEM lamella transfer onto a nickel cantilever for RTS SSRM measurements.

and surface properties, each exhibiting distinct III-V surface reconstructions, growth kinetics and dopant incorporation behavior [22,23]. As illustrated in Fig. 1b, information on the resulting nano-ridge geometry can be routinely obtained using electron microscopy-based techniques, however, predicting the dopant distribution remains far from trivial. Therefore, SSRM can be uniquely positioned as a powerful solution, providing essential feedback in optimization of 3D nano-ridge growth and understanding dopant incorporation and activation mechanisms in GaAs. To this end, SSRM analysis is performed on three different nano-ridge design iterations in this work. The fabrication process of the final optimized GaAs nano-ridge p-i-n laser diode structure, shown in Fig. 1a, is described in more detail in other works [19–23].

2.3. SSRM sample preparation and characterization

The calibration samples were cleaved to create a fresh cross-section, enabling the SPM probe to access the multilayer stack. A gallium indium eutectic-filled scratch on the sample top surface serves as a low-resistive back-contact. For the GaAs nano-ridge structures, cross-sections were prepared using a Sela MC600i micro-cleaving system. The use of a consistent cleaving-based sample preparation approach minimizes cross-section-preparation-induced variations in the near-surface electrical properties probed by SSRM, thereby supporting comparative and quantitative SSRM analysis throughout this study. Focused ion beam (FIB) milling was employed to access the Cu contact layers, followed by local platinum deposition to create back-contact current paths for both n-type and p-type GaAs regions. Fig. 1c shows an optical microscope image of the cleaved nano-ridge cross-section. The SSRM measurements were performed using a Bruker Dimension Icon AFM system equipped with an SSRM application module in an argon environment. Throughout this study, different diamond probes were used, including in-house fabricated boron-doped full diamond tip (FDT) probes in initial stages [24], and commercially available cone shaped coated diamond tip (CDT) probes (Adama innovations, FM-LC) in later measurements. One FA-specific TEM lamella sample was transferred onto a nickel cantilever using a Thermofisher Helios 450 dual-beam FIB/SEM system equipped with a tungsten micromanipulator probe, as illustrated in Fig. 1d, following the protocol proposed by Lagrain et al. [25]. SSRM measurements on the lamella were then performed in the reverse tip sample (RTS) configuration using in-house fabricated hedgehog full diamond tip (HFDT) probe chips [26,27].

3. Optimal SSRM measurement conditions on GaAs

The optimal SSRM measurement conditions on GaAs are determined using the Staircase P and Staircase N calibration samples described in Section 2.1. Fig. 2a shows the layout of both samples, including the ECV-measured carrier concentration for each layer. Particular attention is given to electrical tip–sample interaction, investigated through variation of the tip–sample bias, and to mechanical tip–sample interaction, investigated through the applied force and repeated scanning. Key performance metrics, including dynamic range, repeatability, and doping sensitivity, are evaluated to assess measurement quality. It should be noted that a dedicated tip-to-tip comparison, in which in-house fabricated FDT and commercial Adama CDT probes were systematically evaluated on the same calibration structures under identical measurement conditions, was not performed in this study. Nevertheless, the overall trends discussed in this section were consistently observed across both probe types.

3.1. Electrical tip-sample bias conditions

The impact of the applied tip-sample bias on the SSRM response of GaAs is investigated first, as previous work has demonstrated the importance of carefully selecting the sample bias conditions [15]. To ensure relevance for practical two-dimensional device measurements, the analysis focuses on the I-V characteristics of a dynamic tip-sample contact, i.e. while the tip is scanning over the GaAs surface. Fig. 2b–e shows the SSRM resistance maps obtained on Staircase P and Staircase N at sample biases ranging from +0.5V to +3V and from −0.5V to -3V. The measurements were performed using an applied tip force of approximately 7 µN, representative of typical SSRM operating conditions. Measurements performed at both lower and higher tip load forces showed the same qualitative bias dependence, indicating that the trends discussed below are representative over a wide range of practical SSRM operating forces. For p-type GaAs in forward bias (i.e., a positive p-GaAs bias relative to the tip) (Fig. 2b), a pronounced resistance contrast is observed between the differently doped layers at low sample biases, with a maximum average sensitivity (i.e., slope of the corresponding calibration curve) of 0.94 $\log_{10}(\Omega)$ per decade of carrier concentration over the range covered by Staircase P. However, for biases above +1 V, a significant drop in sensitivity is observed, and it gets harder to distinguish the layers. Under reverse bias conditions (Fig. 2c), the sensitivity is more stable, with values around 1.35 $\log_{10}(\Omega)$ per decade of carrier concentration. Despite the favorable sensitivity, the resistance measured in the semi-insulating GaAs substrate (leftmost region in the resistance map) is slightly lower than that of the 2×10^{17} cm^{-3} doped layer, indicating contrast reversal. This effect is particularly problematic, as

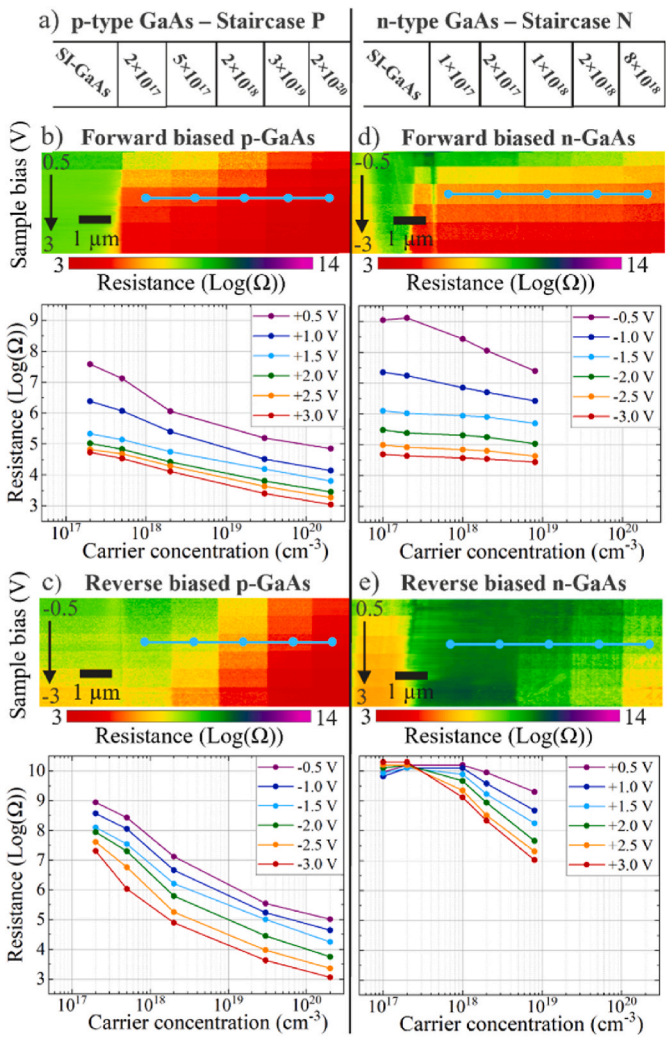


Fig. 2. (a) Layer layout with ECV-measured carrier concentrations of the p-type (Staircase P) and n-type (Staircase N) GaAs calibration samples. SSRM resistance maps of both samples acquired under varying sample bias conditions, ranging from +0.5V to +3V and from −0.5V to -3V in 0.5V increments, together with the corresponding resistance-carrier concentration calibration curves extracted for each bias: (b) Forward biased p-type GaAs, (c) reverse biased p-type GaAs, (d) forward biased n-type GaAs, and (e) reverse biased n-type GaAs. Cyan datapoints corresponding to ±1.5 V are overlaid on the resistance map for visual guidance. (For interpretation of the references to color in this figure legend, the reader is referred to the Web version of this article.)

the extracted calibration curves are used for dopant quantification in unknown samples. This behavior should therefore be carefully taken into account, especially when analyzing low-doped GaAs layers. For n-type GaAs under forward bias (i.e., a negative n-GaAs bias relative to the tip) (Fig. 2d), we observe a sensitivity of 0.88 $\log_{10}(\Omega)$ per decade of carrier concentration at −0.5 V sample bias, and decreasing sensitivity at higher sample biases, similar to the behavior observed in p-GaAs. An opposite trend is observed under reverse bias (Fig. 2e), with increasing sensitivity toward higher sample biases, reaching a maximum of 1.75 $\log_{10}(\Omega)$ per decade of carrier concentration, but at the expense of a complete loss of sensitivity in the lower-doped layers and a more severe contrast reversal in the semi-insulating substrate.

These bias-dependent trends can be understood from the current-transport framework for SSRM on doped III-V semiconductors reported by *Lu* et al. [15], to which we refer for an in-depth discussion of SSRM current transport mechanisms on GaAs. In summary, under forward bias, the SSRM current is primarily governed by thermionic emission across the Schottky-like tip-GaAs barrier, resulting in a positive correlation between current and carrier concentration for both n- and p-type GaAs. Increasing the forward bias further reduces the effective barrier and enhances carrier transmission, thereby reducing the relative influence of carrier-concentration-dependent resistance variations, leading to a lower calibration sensitivity. Under reverse bias, thermionic emission dominates at high carrier concentrations, while generation-recombination current becomes dominant at low doping levels, leading to a reversal of the current-carrier concentration correlation below ~3×10^{17} cm^{-3} in p-type GaAs and an even more pronounced inversion in n-type GaAs. The comparatively weak bias dependence of the reverse-bias sensitivity reflects the interplay between thermionic-emission and generation-recombination current contributions, whose different bias dependences maintain a relatively stable calibration slope in p-GaAs while causing a steeper slope at increased reverse bias in n-GaAs.

In conclusion, for both conductivity types, low forward bias conditions provide the most reliable resistance-to-dopant conversion, maintaining good doping sensitivity and avoiding contrast reversal in the low-doping regime. However, the target application considered in this work involves device structures containing both n-type and p-type GaAs regions. Considering the high sensitivity obtained on p-type GaAs under reverse bias, combined with the less severe contrast reversal compared to reverse-biased n-type GaAs, a sample bias of −1 V is selected for subsequent measurements. This choice enables full device analysis within a single SSRM measurement scan.

3.2. *Mechanical tip-sample interaction conditions*

In addition to sample bias, the mechanical tip-sample interaction force is known to play a crucial role in SSRM, as it defines – together with the tip radius – the contact area, and thereby influences carrier transport across the tip-sample interface. In silicon, SSRM response as a function of force is well studied and marked by a characteristic resistance drop associated with the β-Sn phase transition and the resulting drastic reduction of contact resistance. In contrast, such a clear transition is not expected for GaAs, motivating a brief assessment of the force dependence. Fig. 3a shows resistance maps for Staircase P and Staircase N, obtained at a low force of approximately 1.5 µN and a high force of approximately 10 µN. It is observed that the resistance contrast between different doping levels is substantially improved when measuring at lower forces, with the average sensitivity increasing from 1.36 $\log_{10}(\Omega)$ to 2.34 $\log_{10}(\Omega)$ per decade of carrier concentration for p-type GaAs and from 0.45 $\log_{10}(\Omega)$ to 1.26 $\log_{10}(\Omega)$ per decade for n-type GaAs. The counter-intuitive increase in resistance observed for highly doped n-type GaAs at higher load force may indicate that force-induced surface modification and associated changes in the effective tip–sample contact introduce additional resistance contributions. Especially for SSRM on n-type GaAs, the use of low forces could be a critical solution to significantly improve its intrinsically low sensitivity. This is an important observation as experienced SSRM users are often inclined to move directly to relatively high forces, stemming from the typical SSRM behavior on silicon. Nevertheless, it should be noted that, depending on the tip being used and the sample cross-section condition, an empirical lower-force limit exists, since sufficient force is needed to penetrate surface oxides or other contamination layers in order to reach the onset of thermionic emission current and thereby generate reliable doping contrast. Conversely, higher forces generally improve measurement stability, which is important to prevent current degradation during an SSRM measurement, or between consecutive scans, particularly when calibration measurements are involved. However, the increased tip-sample contact area inevitably leads to a reduced spatial resolution. As a result, the selection of the applied force inherently involves a trade-off between maximizing doping sensitivity while maintaining measurement stability and preserving spatial resolution.

Another important aspect to consider when evaluating SSRM on

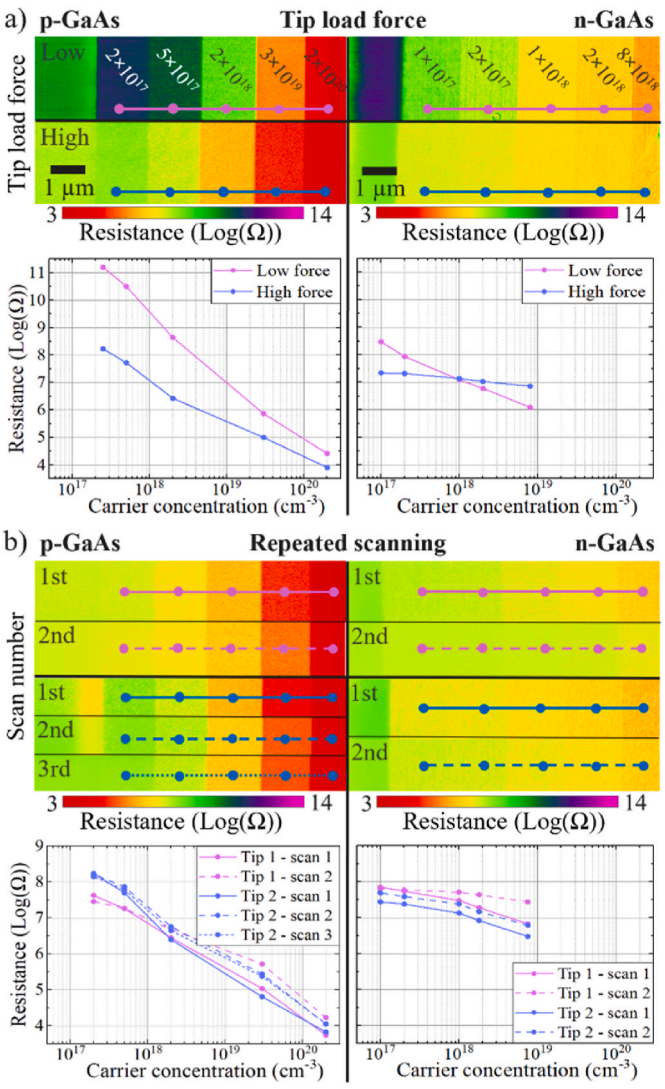


Fig. 3. SSRM resistance maps of p-type and n-type GaAs calibration samples acquired under varying mechanical tip-sample interaction conditions, together with the corresponding resistance-carrier concentration calibration curves extracted for each condition: (a) low and high forces applied to the tip and (b) first, second and third scans over the same area acquired with two different tips.

GaAs is measurement repeatability and tip-to-tip reproducibility. To assess this, consecutive scans were performed under identical measurement conditions and over the same area of Staircase P and Staircase N. Fig. 3b shows the first (solid line) and second (dashed line) scans acquired with each of two different tips. The increase in measured resistance between the first and second scan is consistently observed for both tips and samples and may be attributed to modifications of the near-surface region during the initial scan. These modifications may include mechanically induced changes due to high-pressure scanning, removal or redistribution of surface charge introduced during cross-section preparation, removal of surface oxides or contaminants, and possible scan-induced charging effects. Reduced tip load forces generally result in a smaller resistance shift between the first and second scans, in line with the less pronounced modification of the surface during scanning. The stabilization of resistance values in subsequent scans, as illustrated by the third scan (dotted line) on p-type GaAs acquired with Tip 2, indicates that these modifications largely saturate after the first pass and do not compromise repeatability beyond the first scan. An important implication of these results is that a clear distinction must be made between first and subsequent scans when comparing resistance values across measurements. Although both first and subsequent scans can generally be used to assess doping distributions in GaAs, previously scanned n-type regions occasionally exhibit a reduction in doping contrast, as illustrated by the results obtained with Tip 1.

3.3. Key performance metrics

Having identified a practical operating window for SSRM on GaAs through the bias, force, and repeated-scan studies presented above, the resulting measurement performance can now be evaluated more systematically. The first-scan resistance maps and corresponding resistance-carrier concentration calibration curves obtained with Tip 2 (Fig. 3b) are taken as representative of the typical SSRM response on GaAs, and are therefore used to evaluate several key performance metrics. Firstly, we determine an experimentally validated dynamic range of 2×10^{17} to 2×10^{20} cm^{-3} for p-type GaAs, and of 1×10^{17} to 8×10^{18} cm^{-3} for n-type GaAs, constrained by the limited doping ranges covered in our calibration samples. Literature indicates that the practical dynamic range extends beyond these experimentally validated limits. For n-type GaAs, SSRM contrast has been reported to degrade below 1×10^{17} cm^{-3}, while the upper bound has been demonstrated up to 1.5×10^{19} cm^{-3}. For p-type GaAs, the lower limit can be extended to at least 1×10^{15} cm^{-3} when higher forward bias is applied [15]. Secondly, the steeper slope of the p-type GaAs calibration curve corresponds to a higher SSRM doping sensitivity of approximately 1.5 $\log_{10}(\Omega)$ per decade of carrier concentration, compared to approximately 0.5 $\log_{10}(\Omega)$ per decade for n-type GaAs, consistent with the trends discussed previously. It is worth noting that fast Fourier transform (FFT-)SSRM has been successfully applied to GaAs to further enhance sensitivity, particularly in the higher doping range [28]. Thirdly, the extracted within-layer resistance variability for p-type GaAs ranges from approximately 10% in the highest doped layer to 30% in the lowest doped layer, while for n-type GaAs it remains around 25% across all doping levels. For comparison, a variability of approximately 10% has been reported for silicon in argon environment [14]. This implies that the intrinsic measurement variability of SSRM on GaAs is higher than in Si, which can be attributed to the predominantly Schottky-type tip-sample contact in GaAs, as opposed to the near-ohmic contact achieved in silicon under pressure-induced β-Sn formation. Despite this increase, the observed variability remains sufficiently low to enable differentiation between doping levels, demonstrating that SSRM retains stable measurement performance in GaAs. Moreover, deviations in average layer resistance values between repeated measurements using the same tip, load force, bias, and scan conditions typically remain below 20% when only second or later scans are considered, i.e. after stabilization of the initial scan-induced modification. This value therefore reflects the robust repeatability of SSRM resistance measurements on GaAs under matched conditions. The comparison between the second (dashed line) and third scan (dotted line) on p-type GaAs acquired with Tip 2 (Fig. 3b) can be regarded as representative of this repeatability, while the reported value is based on a total of eight paired calibration measurements, comprising four p-type and four n-type GaAs measurements, each evaluated over five layers. This level of repeatability is critical for practical applications where resistance values are compared across different samples, as well as for quantitative SSRM experiments, in which resistance maps of the target sample must be referenced against calibration measurements. Taking into account the calibration slopes, the 20% resistance variation translates into estimated deviations in extracted carrier concentration of approximately 11% for p-type GaAs and 30% for n-type GaAs under the representative −1 V measurement conditions. These values reflect the intrinsic measurement repeatability under matched calibration and measurement conditions. However, additional contributions, such as tip-related changes or differences in cross-section surface condition may further increase the total uncertainty. Nevertheless, the observed deviations remain within the range typically reported for quantitative SSRM measurements [14], indicating

that calibration curves acquired under identical conditions can be reliably used for resistance-to-carrier concentration conversion in unknown GaAs samples.

4. SSRM for GaAs nano-ridge device metrology

Having established SSRM as a solid carrier profiling technique for GaAs, we now consider a practical metrology use case in which SSRM is employed to provide feedback during the growth optimization of GaAs nano-ridge laser diode devices, leveraging the nano-ridge engineering concept to ensure high material quality in the active device region. Although growth initiated from Si{111} surfaces within narrow oxide trenches of sufficient aspect ratios promotes efficient defect trapping, deposition beyond the trench leads to the formation of a three-dimensional nano-ridge with much more complex growth dynamics. These complexities are largely driven by facet-dependent variations in growth rate, composition and dopant incorporation. Therefore, SSRM is applied to dedicated test structures to spatially resolve these variations and provide a better understanding of the growth process. The analysis is then extended to fully processed GaAs nano-ridge laser diode devices, highlighting the role of SSRM in verifying the device design and advising further optimization. Finally, the applicability of SSRM to reliability and failure analysis is demonstrated through the investigation of electrical stress-induced variations in dopant activation and contact resistivity, and the electrical characterization of localized defects observed in a failure device using the advanced RTS SSRM approach.

4.1. P-type GaAs nano-ridge test structure

Fig. 4 shows cross-sectional scanning electron microscopy (SEM) and SSRM measurements of a carbon-doped (p-type) GaAs nano-ridge structure, grown in five successive growth steps, each performed with constant MOVPE conditions. The expected layer structure and corresponding carbon concentrations, derived from several blanket growth experiments on GaAs substrates and characterized by Van der Pauw Hall measurements and SIMS, are indicated on the SEM image in a simplified, stacked representation. While SEM provides a detailed view of the final nano-ridge morphology and shape, it is not capable of resolving the individual GaAs layers. On the contrary, the 2D SSRM resistance map reveals the presence of seven distinct regions, although only five growth steps were applied during the MOVPE process. This multi-region observation clearly demonstrates that carbon dopant incorporation is not solely determined by the growth parameters, such as temperature and precursor ratios, which remained constant within each step, but are also strongly influenced by the local crystallographic orientation and related surface properties of the growth facets.

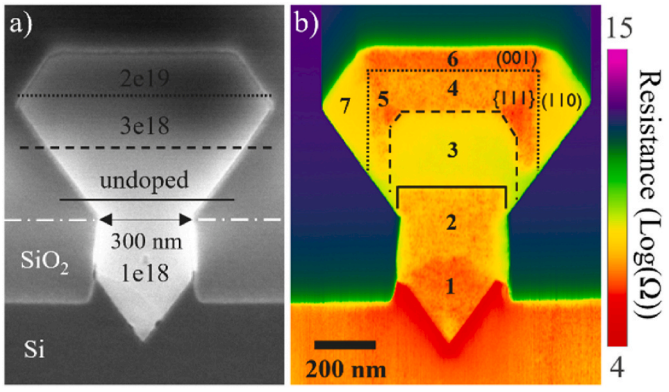


Fig. 4. Cross-section of a carbon-doped (p-type) GaAs nano-ridge test structure: (a) SEM image and (b) 2D SSRM resistance map. The structure is grown in a 300 nm-wide oxide trench initiating from a silicon surface defined by two {111} facets in five steps, each under constant growth conditions. Expected layer structure and intended carbon concentrations are indicated in (a), while distinct regions and growth facets are shown in (b). (For interpretation of the references to color in this figure legend, the reader is referred to the Web version of this article.)

The GaAs nucleation at the bottom of the V-shaped Si trench was performed at very low substrate temperature (350-370 °C) to ensure a continuous two-dimensional III-V seed layer along the two {111} Si facets [29]. Although the exact C concentration has not yet been investigated, such low deposition temperatures are known to promote C incorporation from the group-III precursor. The subsequent deposition of the first layer of interest requires a higher deposition temperature (~600 °C). Since increasing the substrate temperature after seed deposition induces GaAs reflow [29], the material distribution labelled (1) most likely shows this reflow-effect with a lower resistance due to the intrinsic high C-incorporation in the seed layer. MOVPE growth conditions at 600 °C with a C-precursor targeting a C concentration in the 10^{18} cm^{-3} range typically produce box-shaped nano-ridges with a flat (001) top facet. This is consistent with the observed uniform resistance region labelled (2), indicated also by the solid line in Fig. 4b. In the following growth step, the temperature was kept constant but the C precursor was switched off again. The high-resistance region (3) shows that the nano-ridge develops three crystal facets, indicated by the dashed line: (001), {110}, and {111}. This facet evolution reflects a change in the growth-rate hierarchy. In this specific case, the (001) facet grows fastest, promoting the formation of {111} facets. For the next layer of interest, the growth temperature was slightly reduced (and the C-precursor added again) to enhance C incorporation, targeting 3×10^{18} cm^{-3}. A box-shaped nano-ridge forms again, as indicated by the dotted line; however, the 2D SSRM map reveals distinct resistance regions, labelled (4) and (5), where only region (4) matches the expected value of the applied MOVPE step and region (5), grown on top of {111} facets, discloses a lower resistance. These results strongly suggest that the exposed crystal facets affect the C-incorporation efficiency during deposition. Such facet dependence is also observed in the final layer of interest. To further increase the C concentration, the growth temperature was lowered to 500 °C, which enhances the growth rate on {110} facets and leads to the final nano-ridge shape. The low SSRM resistance of the top layer indicates high C concentration, broadly consistent with expectations. However, the triangular nano-ridge edges, labelled (7), exhibit very high resistance, revealing unexpectedly low C incorporation on the {011} facets. It should be noted that SSRM measures the electrically active carrier concentration rather than the total chemical carbon concentration. Therefore, the observed facet-dependent contrast may also reflect differences in dopant activation or compensation, rather than purely variations in chemical carbon incorporation. However, carbon is a shallow acceptor in GaAs and activation efficiencies approaching unity are commonly achieved for optimized MOVPE growth conditions. While hydrogen-related passivation has been reported in some MOCVD-grown GaAs:C layers [30], comparison of SIMS and Hall measurements on blanket calibration layers grown using the same precursor chemistry indicates that hydrogen passivation is negligible in the present material and that the incorporated carbon is activated to a high degree. Therefore, facet-dependent variations in active carrier concentration are expected to predominantly reflect differences in carbon incorporation.

Furthermore, a locally increased resistance is observed near the apex of the V-groove, while a more uniform resistance is measured higher in the trench. A potential explanation could be the high defect density along the III-V/Si interface impacting the carrier mobility. In contrast, the low-resistance silicon region following the V-shaped Si/GaAs interface suggests arsenic in-diffusion from the GaAs during deposition, acting as an n-type dopant in the silicon.

4.2. Fully processed p-i-n GaAs nano-ridge laser diodes

SSRM analysis of test structures has provided valuable insight in the

growth dynamics of GaAs nano-ridges, particularly with respect to dopant incorporation and layer distribution along a 3-dimensional structure in selective area growth. However, it remains to be demonstrated how these findings translate to fully processed GaAs nano-ridge laser diode devices, where n-type, intrinsic and p-type layers are vertically integrated into a single structure. In addition, these devices incorporate InGaAs/GaAs and InGaP/GaAs heterostructures to define the active laser region and surface passivation layer, respectively, as well as tungsten plug contacts to electrically bias the p–i–n diode and enable carrier injection for laser operation. Therefore, SSRM is applied to nano-ridge devices, partly processed for current injection, to assess how the previously identified trends are reflected in device-relevant architectures and to provide unique, spatially resolved carrier profiling feedback throughout their development process. Fig. 5 presents the intended GaAs nano-ridge laser device geometries for three design iterations, together with their corresponding 2D SSRM resistance maps annotated with extracted carrier concentration values for each region, which are used to evaluate the growth process. The carrier concentration values are obtained using a quantitative SSRM data processing workflow [14], in which the resistance-to-carrier calibration curve is derived from SSRM measurements performed on the p-type and n-type GaAs calibration samples Staircase P and Staircase N using the same probe and measurement conditions as those used for the nano-ridge measurement. Since a different probe and applied tip load force were used for each SSRM resistance map, a separate calibration was performed for each nano-ridge design iteration. The applied forces were selected slightly above the empirical lower-force limit required to obtain stable electrical contact and reliable doping contrast for the specific probe, thereby balancing spatial resolution and carrier sensitivity against measurement stability. To further ensure measurement stability and reliability, the calibration measurement was repeated before and after each nano-ridge measurement to verify consistency in the calibration curve and confirm that no significant tip degradation has occurred during the measurement set. Note that Staircase P is Zn-doped, whereas the p-type regions in the GaAs nano-ridges are C-doped. Any difference in hole mobility between both materials will translate directly into the measured spreading resistance and the extracted carrier concentration values. Literature reports indicate that hole mobilities in C- and Zn-doped GaAs are of the same order of magnitude, with C-doped GaAs exhibiting somewhat higher mobilities at high carrier concentrations [31]. Based on the reported mobility differences, the resulting uncertainty in the extracted carrier concentration is expected to remain below 20% over most of the concentration range investigated here, but may increase above 1×10^{19} cm^{-3} reaching up to 75% at 1×10^{20} cm^{-3}. This contribution should be regarded as an additional systematic uncertainty, added on the intrinsic measurement repeatability discussed earlier. Future quantitative SSRM studies on C-doped GaAs devices would ideally employ a C-doped calibration staircase grown under comparable epitaxial conditions, as this would remove the additional dopant-dependent mobility contribution and improve the reliability of absolute carrier concentration extraction. In addition to dopant-dependent mobility differences, structure- and interface-related mobility deviations between the thick epitaxial calibration layers and the GaAs nano-ridge devices may also affect the resistance-to-carrier-concentration conversion. Although a pronounced geometry-induced mobility reduction throughout the several-hundred-nanometer-wide GaAs nano-ridge is not expected, local mobility deviations may occur near the GaAs/Si nucleation region, InGaP/GaAs heterointerfaces, and within the defect-rich ART region. The reported values should therefore be interpreted as effective carrier concentrations obtained under the assumption of calibration-like mobility, with additional local uncertainty expected near interfaces and in defect-rich regions. This mobility limitation is inherent to SSRM calibrations based on reference materials, as the conversion from resistance to carrier concentration reflects both carrier density and mobility.

In the first iteration (Fig. 5a), the nano-ridge device is designed as a

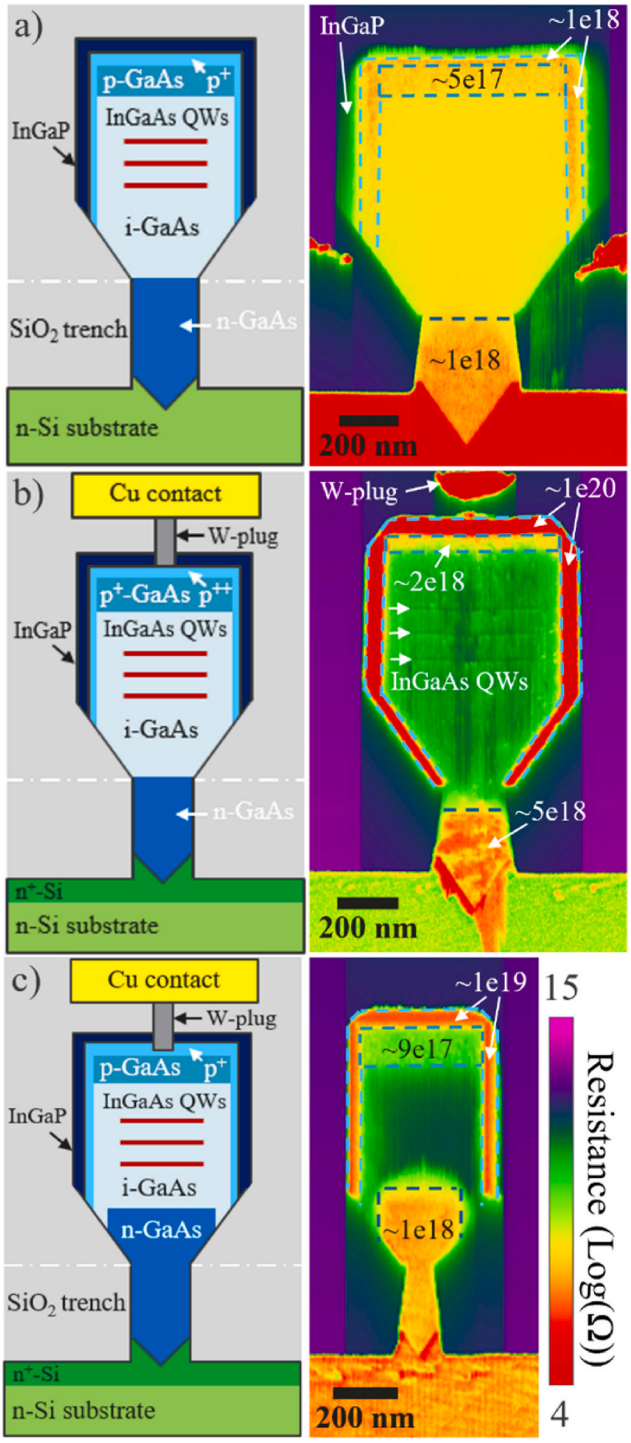


Fig. 5. Schematic cross-sections of the intended GaAs nano-ridge laser device geometries at different design iterations during their development, along with corresponding 2D SSRM resistance maps used to assess the growth process: (a) p-GaAs deposition around the nano-ridge with a very thin p^+-GaAs layer; (b) successful increase in the active doping concentration of the top p^{++}-GaAs layer, but with unintended deposition on the sloped nano-ridge sidewalls; (c) successful growth of n-GaAs out of the oxide trench and selective p-GaAs growth in intended regions only. The color scale is shown only in (c) but applies to all resistance maps in (a)-(c). Overlaid outlines are provided on the SSRM resistance maps to highlight the different doping regions, with colors corresponding to the intended layers in the schematic cross-sections. (For interpretation of the references to color in this figure legend, the reader is referred to the Web version of this article.)

standard vertically stacked p–i–n diode structure, in which the n-type GaAs is confined within the SiO_2 trench, while the p-type GaAs is deposited around the nano-ridge. A thin p^+-GaAs contact layer is included to reduce the contact resistance to the tungsten plug, although the tungsten plug itself is not yet implemented in the first device iteration. The structure is further encapsulated by an InGaP passivation layer covering both the sidewalls and the top edge. The SSRM measurement was performed at a relatively high applied force of 4 μN. The observation of low resistance in the silicon substrate indicates that this force is sufficient to induce the β-Sn phase transition in silicon, confirming excellent tip-sample contact. Consistent with observations across a broader measurement set, the highly resistive InGaP layer can only be reliably distinguished from the surrounding SiO_2 under such elevated forces. In this measurement, the InGaP layer is clearly resolved along the sidewalls with the intended thickness, whereas at the top edge it appears slightly thinner than designed. More critically, the SSRM data provides insight into the carrier distribution of the GaAs regions. The n-type GaAs is successfully confined within the oxide trench, and the p-type GaAs is predominantly located at the top of the nano-ridge, as intended. However, the p^+-GaAs contact layer appears insufficiently doped, as its measured carrier concentration of 1×10^{18} cm^{-3} does not reach the targeted level of 1×10^{19} cm^{-3}, although it should be noted that the absence of the tungsten plug, which would serve as a low-resistance back-contact, introduces an additional parasitic resistance component that is convoluted with the spreading resistance, potentially leading to an underestimation of the actual dopant concentration. Therefore, no strong conclusions are drawn regarding the quantitative carrier concentration levels at this stage.

In the second iteration (Fig. 5b), the tungsten plug and Cu contact layer are implemented, providing a low-resistance back-contact and enabling reliable conversion of the measured resistance into carrier concentration. In addition, the nano-ridge design and growth conditions are adapted based on observations from the first device, including an increase in the doping of the p-GaAs layers. Thanks to the improved contact scheme, SSRM can now confirm a successful enhancement of carriers to 1×10^{20} cm^{-3} in the p^{++}-GaAs layer. However, the latter now extends over the lower sloped {111} sidewalls almost reaching the n-type GaAs bottom layer. A key finding here is that the growth of doped GaAs became more conformal (i.e., less facet dependent) under the applied conditions with increasing doping concentration. This is an important consideration when depositing p-contact layers, as their presence on the sidewalls can increase optical losses and, as they extend toward the n-type bottom layer, increase the risk of reduced carrier injection efficiency into the InGaAs quantum wells. The SSRM measurement was performed at a reduced tip load force of 2.8 μN. Under these conditions, the InGaP layer is not resolved in the resistance map; however, prior transmission electron microscopy (TEM) analysis has confirmed its presence with the intended thickness and conformality. With the lower applied force, the measurement clearly reveals the InGaAs quantum wells, demonstrating the high spatial resolution achievable with SSRM in this regime. Interestingly, this force is well suited to obtain strong carrier contrast between the different GaAs regions, while it is insufficient to induce the β-Sn phase transition in the silicon substrate. This shows that SSRM measurements on GaAs can be effectively performed at a lower force compared to silicon, which is advantageous in terms of both tip lifetime and spatial resolution. Furthermore, a tungsten plug contact is observed in this cross-section. As these contacts are spaced at approximately 5 μm intervals, their appearance in the SSRM measurement depends on the specific cleaving location.

In the final iteration (Fig. 5c), the nano-ridge design is further refined to improve both electrical injection and optical performance, while taking into account limitations in vertical growth control at higher doping levels. The SSRM measurement was performed at a further reduced tip load force of 1.5 μN, yielding sharply defined interfaces and well-resolved edges, thereby demonstrating the excellent spatial resolution achievable under low-force conditions. Despite the reduced load, it remains sufficient to obtain high-quality carrier profiling in GaAs. The n-type GaAs layer is successfully extended to protrude out of the oxide trench, enabling a more continuous electron injection pathway. At the same time, the MOVPE parameters were adjusted so that the p-type GaAs doping concentration is reduced to approximately 1×10^{19} cm^{-3} and to prevent its deposition on the lower sloped sidewalls. Overall, the SSRM result is in excellent agreement with the intended GaAs nano-ridge laser device geometry, confirming that SSRM feedback throughout previous iterations has improved the understanding of MOVPE growth characteristics along a multi-facet 3-dimensional structure and contributed to the realization of functional GaAs p-i-n laser diode devices. Carrier concentrations extracted from SSRM can also be used to support the validation of diode current-voltage models, which can subsequently be employed to further examine device properties and process impacts [32]. Conversely, the multiple interfaces and facets at varying orientations within the nano-ridge structure provide a stringent test for SSRM tip performance. As such, these devices have proven particularly suitable as test samples to evaluate tip sharpness [27].

4.2.1. *Failure analysis in GaAs nano-ridge laser diodes*

To demonstrate that SSRM can serve as a useful tool beyond growth optimization and electrical model validation, a failure analysis case is presented based on a reliability study of fabricated GaAs-on-Si nano-ridge laser diodes [33]. Aging tests were carefully designed to identify the dominant failure mechanisms of the devices. Herein, they are subjected to electrical stress in the form of a constant current above the lasing threshold, while monitoring light-current and current-voltage characteristics over time. In the first phase (<500 h), a gradual increase in threshold current is observed, accompanied by a decrease in overall device resistance. This behavior suggests that, at the onset of stress, local Joule heating near the p-contact plugs – where the current density is highest – acts as an annealing step for the metal/p-GaAs junctions, reducing the effective Schottky barrier height and potentially contributing to further dopant activation in the p-contact layer. To support this hypothesis, Fig. 6a shows comparative 2D SSRM cross-sectional resistance maps of a reference (unstressed) device and a stressed device (mimicking the phase I degradation in Ref. [33]), both fabricated on the same epitaxial structure and chip, with a clear reduction in resistance measured in the p^{++}-GaAs contact layer in the stressed device. This result highlights the capability of SSRM to directly visualize stress-induced changes in contact resistivity and carrier distribution, providing unique insight into device degradation mechanisms.

In a second phase (>500 h), abrupt laser failure occurs, coinciding with diode breakdown and p-contact damage, indicating the formation of a leakage current path impacting the active laser volume. Lock-in thermography, a technique sensitive to localized heat generation due to leakage currents, is used to localize damaged regions, followed by TEM failure analysis at these hot spots. Fig. 6b shows a representative annular dark-field scanning TEM (ADF-STEM) revealing pronounced degradation beneath the W plug. Energy-dispersive X-ray spectroscopy (EDS) identifies interdiffusion, resulting in an As-rich region close to the plug and a small void surrounded by a Ga-rich region penetrating through the upper QW, providing a clear explanation for the abrupt device failure. To further investigate the electrical properties of this defect, the TEM lamella was transferred onto a tipless cantilever, enabling SSRM measurements in RTS configuration. Fig. 6b shows the RTS SSRM resistance map, clearly indicating a localized increase in resistance within the low-density area of the defect whereas the surrounding Ga-rich region exhibits a slightly reduced resistance. In the context of this work, the result demonstrates the distinct capability of RTS SSRM to perform site-specific resistance measurements on TEM-prepared samples, enabling detailed electrical characterization of localized failure mechanisms that are not accessible using the

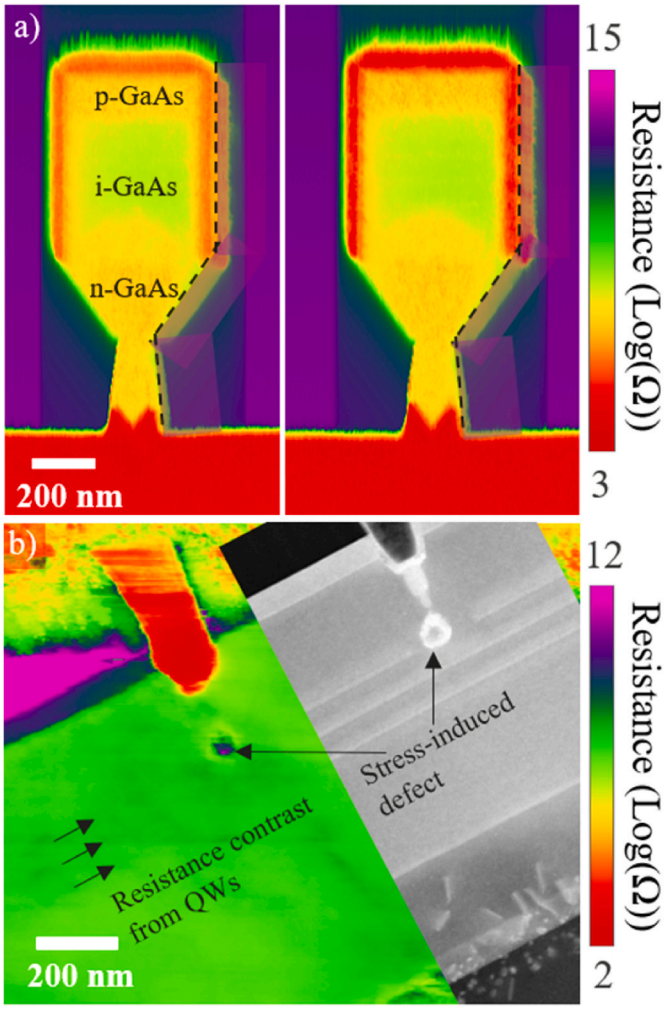


Fig. 6. (a) 2D cross-sectional SSRM resistance maps of a reference GaAs nano-ridge laser device (left) and a device that has been electrically stressed and shows a reduced device series resistance (right). (b) 2D SSRM resistance map overlaid with an ADF-STEM image of a cross-section along the nano-ridge direction at a stress-induced defect location. The SSRM measurement is performed in RTS configuration on the TEM lamella.

conventional SSRM configuration.

5. Conclusions

In this work, we have established SSRM as a robust and practical technique for quantitative two-dimensional carrier profiling in advanced GaAs-based devices. Through a systematic study of electrical and mechanical tip-sample interactions, an optimized operating window for SSRM on GaAs was identified. A strong bias dependence of the SSRM response was confirmed, with low forward-bias conditions providing the most reliable resistance-to-carrier conversion when considering p- and n-type GaAs separately, while a sample bias of −1 V was selected as an optimal compromise for simultaneous characterization of both conductivity types in a single measurement. Reduced tip load forces were further found to significantly improve resistance contrast, whereas a systematic increase in resistance between the first and second scan, followed by stable resistance values in subsequent scans, marks the need to distinguish between first and subsequent scans during data interpretation and calibration. Under these optimized conditions, SSRM on GaAs provides dynamic ranges spanning at least 2×10^{17} to 2×10^{20} cm^{-3} for p-type GaAs and 1×10^{17} to 8×10^{18} cm^{-3} for n-type GaAs. Doping sensitivities of approximately 1.5 and 0.5 $\log_{10}(\Omega)$ per decade of carrier concentration were obtained for p- and n-type material, respectively, and within-layer resistance variability ranging from 10% in highly doped layers to 30% in lowly doped layers for p-type GaAs, compared to a constant variability of approximately 20% for n-type GaAs. Together with measurement-to-measurement variations in average layer resistance below 20%, these results assure that SSRM provides stable and repeatable measurements suitable for reliable resistance-to-carrier concentration conversion in both p- and n-type GaAs, with particularly high sensitivity in p-type material. The practical value of SSRM was demonstrated on monolithically integrated GaAs nano-ridge laser diodes grown on silicon, where it provided direct insight into facet-dependent growth characteristics, dopant incorporation, and dopant activation. The resulting carrier profiling feedback enabled optimization of the spatial distribution and concentration of p- and n-type regions, which is critical for minimizing contact resistance, optical losses, and leakage currents while ensuring efficient carrier injection and transport toward the quantum wells. In addition, SSRM was applied to failure analysis, revealing electrical stress-induced resistance changes in the p-GaAs contact layer consistent with a contact-annealing mechanism during early device operation, while RTS SSRM enabled site-specific electrical characterization of a localized degradation defect initially identified by TEM. We believe that the measurement guidelines, performance assessment, and application examples presented in this work can provide a practical framework for the broader adoption of SSRM in GaAs-based technologies.

CRediT authorship contribution statement

L. Wouters: Writing – original draft, Visualization, Methodology, Investigation, Conceptualization. **P. Lagrain:** Writing – review & editing, Investigation. **N. Peric:** Writing – review & editing, Investigation. **P. Y. Hsieh:** Writing – review & editing, Methodology, Investigation. **P. Swekis:** Writing – review & editing, Investigation. **A.M.R. Sharma:** Investigation. **Y. Mols:** Investigation. **I. De Wolf:** Writing – review & editing, Supervision. **B. Kunert:** Writing – review & editing, Methodology, Investigation, Conceptualization. **T. Hantschel:** Writing – review & editing, Supervision.

Declaration of competing interest

The authors declare that they have no known competing financial interests or personal relationships that could have appeared to influence the work reported in this paper.

Data availability

Data will be made available on request.

References

[1] M.R. Brozel, G.E. Stillman, Properties of gallium arsenide, Electr. Mater. Inform. Service 16 (1996).
[2] S. Mokkapati, C. Jagadish, III-V compound SC for optoelectronic devices, Mater. Today 12 (2009) 22–32, https://doi.org/10.1016/S1369-7021(09)70110-5.
[3] J.A. Del Alamo, Nanometre-scale electronics with III-V compound semiconductors, Nature 479 (2011) 317–323, https://doi.org/10.1038/nature10677.
[4] O. Esame, Y. Gurbuz, I. Tekin, A. Bozkurt, Performance comparison of state-of-the-art heterojunction bipolar devices (HBT) based on AlGaAs/GaAs, Si/SiGe and InGaAs/InP, Microelectronics J 35 (2004) 901–908, https://doi.org/10.1016/j.mejo.2004.07.003.
[5] W. Vandervorst, et al., Dopant, composition and carrier profiling for 3D structures, Mater. Sci. Semicond. Process. 62 (2017) 31–48, https://doi.org/10.1016/j.mssp.2016.10.029.
[6] T. Clarysse, et al., Accurate carrier profiling of n-type GaAs junctions, Mater. Sci. Semicond. Process. 11 (2008) 259–266, https://doi.org/10.1016/j.mssp.2008.11.010.
[7] P.P. Michałowski, et al., Artifact-free secondary ion mass spectrometry profiling of a full vertical cavity surface emitting laser structure, Measurement 225 (2024), https://doi.org/10.1016/j.measurement.2023.114003.
[8] V. Karki, D. Bhattacharya, T.V. Chandrasekhar Rao, D. Alamelu, Depth distribution of Mn in Mn doped GaAs using secondary ion mass spectrometry, J. Vacuum Sci.

Technol. B Nanotechnol. Microelectr.: Mater. Process. Measurement Phenomena 34 (2016), https://doi.org/10.1116/1.4943948.
[9] A. Franquet, V. Spampinato, S. Kayser, W. Vandervorst, P. van der Heide, Orbitrap^{TM}-SIMS analysis of advanced semiconductor inorganic structures, Vacuum 202 (2022) 111182, https://doi.org/10.1016/J.VACUUM.2022.111182.
[10] D.K. Schroder, Semiconductor Material and Device Characterization, Wiley, 2005, https://doi.org/10.1002/0471749095.
[11] Enrico Di Russo, François Vurpillot, Lorenzo Rigutti, Compositional Metrology of Atom Probe Applied to Non-metallic Materials, 2026, https://doi.org/10.48550/arXiv.2602.14565.
[12] S.B. Kuntze, D. Ban, E.H. Sargent, S.J. Dixon-Warren, J.K. White, K. Hinzer, Electrical scanning probe microscopy: investigating the inner workings of electronic and optoelectronic devices, Crit. Rev. Solid State Mater. Sci. 30 (2005) 71–124, https://doi.org/10.1080/10408430590952523.
[13] A. Schulze, et al., Mapping conductance and carrier distributions in confined three-dimensional transistor structures, in: U. Celano (Ed.), Electrical Atomic Force Microscopy for Nanoelectronics, Springer, Cham, 2019, pp. 71–106, https://doi.org/10.1007/978-3-030-15612-1.
[14] M.A.R. Laskar, et al., The enduring legacy of scanning spreading resistance microscopy: overview, advancements, and future directions, Appl. Phys. Rev. 12 (2025), https://doi.org/10.1063/5.0280969.
[15] R.P. Lu, K.L. Kavanagh, St J. Dixon-Warren, A.J. SpringThorpe, R. Streater, I. Calder, Scanning spreading resistance microscopy current transport studies on doped III–V semiconductors, J. Vac. Sci. Technol. B: Microelectr. Nanometer Struct. Process. Measurement Phenomena 20 (2002) 1682–1689, https://doi.org/10.1116/1.1496512.
[16] A. Szyszka, B. Ściana, D. Radziewicz, W. Macherzyński, B. Paszkiewicz, M. Tłaczała, Characterization of A III B V epitaxial layers by scanning spreading resistance microscopy, Opt. Appl. 41 (2011).
[17] L. Qiang, et al., Indepth doping assessment of thick doped GaAs layer by scanning spreading resistance microscopy, J. Appl. Phys. 136 (2024), https://doi.org/10.1063/5.0215140.
[18] R.P. Lu, et al., Calibrated scanning spreading resistance microscopy profiling of carriers in III–V structures, J. Vac. Sci. Technol. B: Microelectr. Nanometer Struct. Process. Measurement Phenomena 19 (2001) 1662–1670, https://doi.org/10.1116/1.1387458.
[19] Y. De Koninck, et al., GaAs nano-ridge laser diodes fully fabricated in a 300-mm CMOS pilot line, Nature 637 (2025) 63–69, https://doi.org/10.1038/s41586-024-08364-2.
[20] D. Van Thourhout, et al., Nano-ridge laser monolithically grown on (001) Si, Semiconduct. Semimet. 101 (2019) 283–304, https://doi.org/10.1016/bs.semsem.2019.07.002.
[21] B. Kunert, et al., III/V nano ridge structures for optical applications on patterned 300 mm silicon substrate, Appl. Phys. Lett. 109 (2016), https://doi.org/10.1063/1.4961936.
[22] B. Kunert, W. Guo, Y. Mols, R. Langer, K. Barla, Integration of III/V Hetero-Structures By Selective Area Growth on Si for Nano- and Optoelectronics, ECS Trans. 75 (2016) 409–419, https://doi.org/10.1149/07508.0409ecst.
[23] W.I. Wang, E.E. Mendez, T.S. Kuan, L. Esaki, Crystal orientation dependence of silicon doping in molecular beam epitaxial AlGaAs/GaAs heterostructures, Appl. Phys. Lett. 47 (1985) 826–828, https://doi.org/10.1063/1.95997.
[24] T. Hantschel, et al., Diamond scanning probes with sub-nanometer resolution for advanced nanoelectronics device characterization, Microelectron. Eng. 159 (2016) 46–50, https://doi.org/10.1016/j.mee.2016.02.053.
[25] P. Lagrain, et al., Enabling focused ion beam sample preparation for application in reverse tip sample scanning probe microscopy, Micro Nano Eng. 23 (2024), https://doi.org/10.1016/j.mne.2024.100247.
[26] H.S. Kim, et al., Probe chip nanofabrication enabled reverse tip sample scanning probe microscopy concept and measurements, Nanotechnology 35 (2024), https://doi.org/10.1088/1361-6528/ad3744.
[27] L. Wouters, et al., Nanofabrication of sharp conductive diamond tip probe chips and their application in reverse tip sample scanning probe microscopy, Micro Nano Eng. 28 (2025), https://doi.org/10.1016/j.mne.2025.100307.
[28] O. Dixon-Luinenburg, U. Celano, W. Vandervorst, K. Paredis, Carrier profiling with fast fourier transform scanning spreading resistance microscopy: a case study for Ge, GaAs, InGaAs, and InP, Ultramicroscopy 206 (2019), https://doi.org/10.1016/j.ultramic.2019.06.009.
[29] W. Guo, et al., Anisotropic relaxation behavior of InGaAs/GaAs selectively grown in narrow trenches on (001) Si substrates, J. Appl. Phys. 122 (2017), https://doi.org/10.1063/1.4991481.
[30] S.A. Stockman, et al., Passivation of carbon acceptors during growth of carbon-doped GaAs, InGaAs, and HBTs by MOCVD, J. Electron. Mater. 21 (1992), https://doi.org/10.1007/BF02667602.
[31] S.A. Stockman, et al., Characterization of heavily carbon-doped GaAs grown by metalorganic chemical vapor deposition and metalorganic molecular beam epitaxy, J. Appl. Phys. 72 (1992) 981–987, https://doi.org/10.1063/1.1351776.
[32] P.Y. Hsieh, et al., Advanced current-voltage model of electrical contacts to GaAs- and Ge-Based active silicon photonic devices, IEEE Trans. Electron. Dev. 70 (2023) 4274–4279, https://doi.org/10.1109/TED.2023.3285711.
[33] P.Y. Hsieh, et al., Degradation mechanisms of monolithic GaAs-on-Si nano-ridge quantum well lasers, J. Lightwave Technol. 43 (2025) 5811–5819, https://doi.org/10.1109/JLT.2025.3557373.